Ultrasound in Med. & Biol., Vol. 25, No. 7, pp. 1099–1113, 1999
Copyright © 1999 World Federation for Ultrasound in Medicine & Biology
Printed in the USA. All rights reserved
0301-5629/99/$–see front matter

PII S0301-5629(99)00044-7

● *Original Contribution*

ELASTOGRAPHIC CHARACTERIZATION OF HIFU-INDUCED LESIONS IN CANINE LIVERS

RAFFAELLA RIGHETTI,[†‡] FAOUZI KALLEL,[†] R. JASON STAFFORD,[*] ROGER E. PRICE,[§] THOMAS A. KROUSKOP,[‖] JOHN D. HAZLE[*] and JONATHAN OPHIR[†]

[†]The University of Texas Medical School, Department of Radiology, Ultrasonics Laboratory, Houston, TX 77030 USA; [‡]Electronic Engineering Dept., University of Florence, 50139 Firenze, Italy; [*]The University of Texas M. D. Anderson Cancer Center, Section of Diagnostic Imaging Physics and [§]Department of Veterinary Medicine and Surgery, Houston, TX 77030 USA; and [‖]Baylor College of Medicine, Department of Physical Medicine and Rehabilitation, Houston, TX 77030 USA

(*Received* 18 *November* 1998; *in final form* 26 *March* 1999)

Abstract—The elastographic visualization and evaluation of high-intensity focused ultrasound (HIFU)-induced lesions were investigated. The lesions were induced *in vitro* in freshly excised canine livers. The use of different treatment intensity levels and exposure times resulted in lesions of different sizes. Each lesion was clearly depicted by the corresponding elastogram as being an area harder than the background. The strain contrast of the lesion/background was found to be dependent on the level of energy deposition. A lesion/background strain contrast between −2.5 dB and −3.5 dB was found to completely define the entire zone of tissue damage. The area of tissue damage was automatically estimated from the elastograms by evaluating the number of pixels enclosed inside the isointensity contour lines corresponding to a strain contrast of −2.5, −3 and −3.5 dB. The area of the lesion was measured from a tissue photograph obtained at approximately the same plane where elastographic data were collected. The estimated lesion areas ranged between approximately 10 mm^2 and 110 mm^2. A high correlation between the damaged areas as depicted by the elastograms and the corresponding areas as measured from the gross pathology photographs was found ($r^2 = 0.93$, p value < 0.0004, $n = 16$). This statistically significant high correlation demonstrates that elastography has the potential to become a reliable and accurate modality for HIFU therapy monitoring. **© 1999 World Federation for Ultrasound in Medicine & Biology.**

Key Words: **Elastography, HIFU, Minimally invasive surgery, Strain, Tissue ablation, Ultrasound.**

INTRODUCTION

It has been known since the early 1950s that focusing high-intensity ultrasound beams can heat or destroy volumes of tissue at depths up to 10 cm and at exposure times on the order of seconds (Fry et al. 1950, 1954; Lele 1967). This technique is usually referred to as high-intensity focused ultrasound (HIFU) or focused ultrasound surgery (FUS), and falls within the category of minimally invasive surgical modalities. The energy source is situated outside the body and, consequently, no surgical incision is required.

The first HIFU studies and experiments were limited only to neurological and neurosurgical applications, for which high precision and tissue selectivity were required (Lynn and Putnam 1944; Fry et al. 1954; Fry and Fry 1960). In those cases, the pathway of the ultrasonic beam was created by removing a portion of the skull overlying the region to be sonicated. Only recently, after the further development of hyperthermia modalities, the possibility of using this technology for the ablation of tumors in soft tissue has been considered (Fry and Johnson 1978; Corry et al. 1984). The lack of an imaging technique that was able to accurately and reliably guide the ultrasonic beam during treatment was the biggest impediment to *in vivo* applications of HIFU until the late 1970s. The development of magnetic resonance imaging (MRI) methods to monitor temperature changes in the target region in real-time has marked a turning point in the history of HIFU (Cline et al. 1995; Hynynen et al. 1996; Hynynen 1996). Although MR imaging has been proven to be quite adept at guiding focused ultrasound surgery, it has its own drawbacks and limitations. MRI is expensive, not portable and may not be suitable for some

Address correspondence to: Faouzi Kallel, Department of Radiology, Ultrasonics Laboratory, University of Texas Medical School, 6431 Fannin St., Houston, TX 77030 USA. E-mail: fkallel@msrad3.med.uth.tmc.edu

patient populations, such as those with pacemakers, pregnant women, children or very large patients.

The fundamental concept of HIFU is to create irreversible necrosis in a target volume of tissue, while avoiding damage to the surrounding tissue. The volume of damaged tissue is conventionally called a "lesion." In the case of a thermal lesion, the extent of the damage depends on the temperature level reached and the exposure time (thermal dose) (Vykhodtseva et al. 1994; ter Haar 1995; Sanghvi et al. 1996). Detailed studies established some temperature levels as conventional "thresholds" for the formation of HIFU lesions (Hill et al. 1994; Hynynen 1996), suggesting a temperature threshold of 58–60°C at the border of the lesion. The primary mechanism of damage associated with the formation of a HIFU lesion is a thermal one. However, depending on the intensity and the exposure time, other damage mechanisms may be involved. For example, when the temperature of the tissue reaches the vaporization threshold level of the water (100°C), the water in the tissue begins to boil, resulting in the formation of gas bubbles and, therefore, in a rapid volume expansion that destroys the cells explosively (McKenzie 1990). When this happens, the damage mechanism is not only thermal, but mechanical as well. The same type of damage mechanism is also involved when cavitation occurs. The mechanical damage mechanism is considered to be more violent and more effective than the thermal one (Wells 1977; Prat et al. 1991, 1994; Cathignol et al. 1995). Consequently, lesions for which the temperature exceeded 100°C, or those in which cavitation occurred, generally show a different shape and appearance compared to lesions created by a purely thermal damage mechanism (Hill and ter Haar 1995; Malcolm and ter Haar 1996; Chapelon et al. 1999).

For many years, the possibility of using standard ultrasound imaging techniques to detect and visualize lesions induced by HIFU has been considered (Lele 1966; ter Haar et al. 1989; Yang et al. 1993). This would have reduced the costs required for MRI-guided FUS and given more mechanical compatibility. It has been reported that the acoustic properties of tissue change during heating, as well as after the formation of the lesion (Bush et al. 1993; Gertner et al. 1997; Ribault et al. 1998). In particular, it has been shown that thermal damage is associated with a significant increase of the attenuation coefficient and the speed of sound. Unfortunately, it was also reported that the backscatter coefficient does not change in any significant manner (Bush et al. 1993). Thus, the potential of ultrasonography to guide focused ultrasound surgery has yet to be proven. Indeed, standard ultrasonic methods seem to be insufficiently accurate for the detection of purely thermal lesions (Hill and ter Haar 1995; ter Haar 1995; Hynynen 1997). Only in a few cases the lesions appeared in conventional sonograms as hyperechoic regions (Hynynen 1991). This was presumably related to the formation of gas bubbles due to vaporization and/or cavitation (Hynynen 1991; Gertner et al. 1998). However, even in these cases, the extent of the damage was seriously underestimated from the sonograms. Moreover, the increased echogenicity of the treated areas tended to fade with time (Watkin et al. 1995), presumably due to the resorption of the bubbles.

Yang et al. (1993) have shown that, immediately after the treatment, HIFU-induced damage in rabbit liver *in vivo* was depicted as hypoechoic lesions. They related the decreased echogenicity in the lesion to increased water content due to tissue edema. They also reported that, as a result of calcium deposition and condensation of nuclear debris from the infiltrating leukocytes around the lesion periphery, a hyperechoic rim was seen around the margin of the lesion 4 days after treatment.

A serious complication of ultrasonically monitored HIFU treatment of tumors is the intrinsically poor visualization of certain tumors by sonography. For example, focal breast masses may have echogenicities that are similar to those of surrounding fatty tissue (Garra et al. 1997). In the prostate, 23% to 25% of the cancers are isoechoic (Norberg et al. 1993). In these cases, sonography may not be appropriate for guiding focused ultrasound surgery.

Recently, methods to map information related to the elastic properties of soft tissues have been proposed, as reviewed by Gao et al. (1996). Elastography, first introduced by Ophir et al. (1991), is one of these techniques. The principle of elastography consists of acquiring RF signals from the tissue before and after the application of a small surface compression (displacement). The resulting internal tissue displacements are then computed using cross-correlation techniques applied to pre- and post-compression RF data segments. The local axial tissue strains (gradient of the estimated displacement field) are then displayed as an image termed an elastogram; generally, soft tissues undergo more strain than harder tissues. The measured strain is related to the tissue shear modulus that is dependent on the high level of tissue organization (Sarvazyan et al. 1993). The tissue acoustic properties, on the other hand, are primarily related to tissue bulk modulus and density and, thus, to their molecular composition. Therefore, it is expected that elastography may convey new information that overcomes the limitation of conventional sonography in the visualization of isoechoic tumors. This has been successfully demonstrated *in vivo* (Garra et al. 1997).

It is known that protein denaturation induces elevation of the elastic modulus of proteins and of soft tissue (Fasano et al. 1983; Consigny et al. 1989; Kang et al. 1995). It is, therefore, expected that the elastic modulus

of the tissue would change as a consequence of heat-induced denaturation as well. Chen and Humphrey (1998) studied the stress-strain behavior of a collagenous tissue undergoing different extents of prior thermal damage. They showed that the heat-induced changes of the mechanical properties are only related to the extent of the prior damage and do not depend on the specific thermo-mechanical history that caused the damage. They also reported a gradual increase in the tissue stiffness following thermal damage.

We have recently shown the feasibility for visualizing Laser-induced thermal lesions with elastography (Stafford et al. 1998). Because, as shown by Chen and Humphery (1998), the heat-induced changes are independent of the specific thermo-mechanical history that caused the damage, it is reasonable to hypothesize the feasibility of elastographic visualization of HIFU-induced lesions. This has been demonstrated in a recent preliminary study by Kallel et al. (1999), who have shown accurate elastographic visualization of HIFU-induced lesions in rabbit paraspinal muscles.

Recently, new ultrasonic techniques for beam guidance by the mean of temperature mapping were proposed (Ueno et al. 1990; Straube and Arthur 1994; Seip and Ebbini 1995; Moreno et al. 1995; Simon et al. 1998). The combination of one of these techniques with elastography could lead to an entirely ultrasound-based HIFU system.

The objectives of this study were to characterize the elastographic appearance of HIFU-induced lesions and to evaluate the correlation between elastographic and pathological measurements of the areas of HIFU-induced lesions.

MATERIALS AND METHODS

Tissue sample handling and lesion generation

Thermal lesions were induced in fresh, excised canine livers using a prototype MR-compatible high-intensity focused ultrasound surgery system (GE Medical Systems, Milwaukee, WI) (Cline et al. 1995; Hynynen et al. 1996; Hynynen 1996). The livers were harvested from mongrel dogs being used for a different study. Appropriately sized portions of the liver lobes were excised, immersed in an isotonic saline solution and stored at approximately 4°C for not more than 24 h before the sonication.

This MR-compatible HIFU system uses a single, spherical, air-backed transducer operating at a center frequency of approximately 1.5 MHz, with an 80-mm radius of curvature and 100-mm diameter, to generate the focused ultrasound field. The transducer was placed in a sealed watertight Plexiglas tank of degassed water (Degas Model B2L2P, Intec Research, Sunnyvale, CA) to provide acoustic coupling between the transducer and the tissue sample. A thin plastic film (0.1 mm thick polyvinylchloride) enclosed the water tank. To align the MR coordinate system with the transducer coordinate system, a gelatin phantom (3M, Minneapolis, MN), that mimics the ultrasonic properties of tissue was placed in the center of an MR surface coil above the transducer. The center of the transducer was aligned with the axial center of the 1.5 T MR scanner. A low power sonication pulse was delivered to the phantom (20 W RF power) and a thermally sensitive fast spin-echo sequence was acquired simultaneously. A change of state in the phantom at 57°C allows the position of the focal spot to be determined in the MR coordinate system accurately (Cline et al. 1993). After the coordinate systems were registered, the phantom was removed and the tissue sample was positioned on top of the tank in a Plexiglas holder filled with degassed water. Prior to the treatment, each sample was placed in a constant temperature water bath until the temperature of the sample reached an approximate value of 25°C (after approximately 10 min). A 100-mm diameter radiofrequency (RF) surface coil was placed on top of the tissue sample. To reduce motion of the tissue sample, the coil was taped to the Plexiglas holder (Fig. 1). To prevent tissue from drying during the treatment, the samples were completely submerged in degassed water. To properly choose the treatment plane, a contiguous set of T2-weighted coronal MR cross-sections covering the entire region of treatment and containing the ultrasonic focal plane were acquired. This plane was usually selected to have a small number of blood vessels and a depth suitable to assure that the lesion would not be superficial. Online monitoring of the treatment was ac-

Fig. 1. Plexiglas tissue sample holder positioned above the HIFU transducer. The liver specimen is positioned in a water bath and completely covered by degassed water. A circular RF coil is placed on top of the tissue sample and taped to the holder to minimize motion.

complished using a temperature-sensitive, fast, 2D RF spoiled gradient-recalled acquisition (SPGR) pulse sequence (TE/TR/flip = 4 ms/9.7 ms/25°, 0.6 s per image) with a 14 cm^2 field of view in the prescribed plane and a 256 × 64 reconstruction matrix. This pulse sequence allowed the changes in the proton resonance frequency of the tissue to be monitored during temperature changes, by taking the complex phase difference of an initial reference image and subsequent images acquired during therapy (Chung et al. 1996). This, in turn, allowed placement of the focus in the sample to be monitored during treatment and estimations of the temperature rise in this region to be calculated off-line.

All the lesions were generated by exposing the tissue to an *in situ* spatially averaged focal intensity ranging between 750 W cm^{-2} and 1565 W cm^{-2} and sonication-time variable from 8 to 20 s. This permitted us to obtain lesions of different sizes and shapes, each of them created by a single exposure of the sample to the ultrasonic beam. It has to be noticed that such values of sonication parameters are atypical for clinical HIFU treatment where usually shorter exposures are used. The *in situ* spatially averaged focal intensity (defined as I_{SAL} by Hill et al. 1994) was calculated using the equation:

$$I_{SAL} = 0.867 \frac{W}{D^2}, \quad (1)$$

where D is the −6 dB beam dimension (~2 mm in our system) and W is the acoustic power output of the transducer, calculated from the RF power, assuming an efficiency of the transducer of 60% (Cline et al. 1994). As discussed by Hill et al. (1994), the use of eqn (1) is based on the simplifying assumption of linear conditions of acoustic propagation in a nonattenuating medium. In practice, the intensity value predicted by eqn (1) should be derated to account for the appropriate attenuation coefficient in the medium. For the purpose of this paper, because the precise knowledge of the spatially averaged focal intensity *in situ* is not necessary, no correction for ultrasound attenuation was considered.

Immediately after the creation of the thermal damage, coronal and axial T2-weighted MR images were acquired to verify the extent of the damage. These images were subsequently used to guide the elastographic data acquisition.

Elastographic data acquisition

Each sample was cast in a block of clear gelatin prepared as described by Kallel et al. (1998). The gelatin block was placed in the compression apparatus. A square compression plate larger than the size of the gelatin block sample was used to maintain a uniform applied axial stress distribution. The experiments were conducted using a real-time linear array scanner (Diasonics Spectra II, Santa Clara, CA) that operates with dynamic receive focusing and a single transmit focal zone centered around 30 mm, a center frequency of 5 MHz and a 40-mm aperture. The linear array transducer was coupled to the gelatin sample *via* an opening in the metal plate. Each sample was scanned in planes perpendicular and parallel to the axis of the ultrasonic treatment beam. The transducer was initially positioned on the edge of the sample inside the block of gelatin and sequentially moved laterally across the sample in steps of 1 mm. The region of interest (ROI) for most elastograms was 55 mm along the longitudinal beam axis. For all elastograms, 100 A-lines were used. Precompression strain of each sample ranged from 0.2% to 4%. A maximum of 3 compression steps for each scan, with a compression step size of 0.5 mm (compressor/transducer axial motion) for most samples, was used. This applied displacement resulted in a 0.5% average applied strain for each step. The RF signals for each step were digitized using an 8-bit digitizer (Lecroy Corp., Chestnut Ridge, NY) operating at a sampling frequency of 48 MHz, and saved to a desktop computer for off-line processing.

Local tissue displacements were estimated using cross-correlation techniques applied on pre- and post-compression digitized radiofrequency echo A-lines from the region of interest. For all elastograms, the length of the correlation windows, both for the pre- and postcompression signals, was fixed to a value of 2 mm with a 75% window overlap. The choice of these parameters resulted in a compromise between spatial resolution and contrast-to-noise ratio (CNR) (Varghese and Ophir 1998), which in elastography is computed from the means and variances of the strains in the lesion and the background, respectively (Bilgen and Insana 1997). The local longitudinal strain was estimated from the displacement data using a least squares strain estimator (LSQE) with a kernel size of ~4 mm. This permitted the generation of elastograms characterized by high signal-to-noise ratio and CNR, with a relatively small loss of spatial resolution (Kallel and Ophir 1997).

Mechanical measurements

Mechanical measurements of the elastic modulus of the tissue of two HIFU-induced lesions were performed using a hydraulic servo Instron testing machine (Instron, Inc., Canton, MA). The lesions were induced in the sample using an *in situ* spatially averaged focal intensity of 750 W cm^{-2} and 1378 W cm^{-2} and an exposure time of 20 s, following the same procedure previously described. The distance between the centers of the two lesions was approximately 2.5 cm. The sample was then uniformly cut into 4-mm thick slices. Two slices were

tested using an applied strain level ranging between 0 to 5% at a rate of 1% per s. The indentor was 2.43 mm in diameter. The acquired force and displacement data were then used to generate the stress-strain curves representing the tissue in the center of the two lesions and in the normal tissue (background). The slope of these curves determined the elastic moduli of the selected regions for a range of applied strain (Krouskop et al. 1998). Immediately after the Instron measurements, the same slices were cast in a clear block of gelatin and elastographic data were acquired as described previously. The resulting elastograms were used to compute the lesion/background strain contrasts.

Pathology

After elastographic data acquisition, each sample was removed from the gelatin block and fixed by immersion in a 10% buffered neutral formalin solution. The fixed sample was sliced in a plane comparable to the plane in which elastographic data were acquired. Each slice was approximately 2–3 mm thick. Composite photographs of all the tissue slices and selected individual slices that contained grossly visible lesions were obtained to document the gross pathology observed. A centimeter scale was included in each tissue photograph. Histological evaluation of hematoxylin- and eosin-stained $4-6$ μm sections was performed for two different lesions.

Evaluation and characterization of the lesions

The entire damaged area was used as a parameter to quantify the potential of elastography in evaluating HIFU-induced thermal lesions. For each lesion, the area of grossly visible tissue damage as measured from the corresponding tissue photograph was correlated with the extent of the lesion in the elastogram that was automatically depicted using computer-generated isointensity contour plots. This approach is objective when compared to the procedure based on the use of human observers. The measurement does not suffer from fluctuations introduced by inherent observer subjectivity. All the elastograms were displayed using a fixed strain dynamic range of 0%–2%. The average strain in a homogeneous tissue region far from the lesion was computed for each elastogram. This average strain was then used to normalize the elastograms to the same level. This level was arbitrarily fixed to 1%. This step is necessary to obtain consistent depiction of the damaged areas using one particular isointensity contour level. This is possible as long as the lesion/background modulus contrast does not change within a given applied strain range. Actual measurement of the elastic modulus using an Instron testing machine confirmed this hypothesis.

Preliminary experiments and simulations were used to determine the value of strain contrast (isointensity contour level) that best enclosed the entire area of damaged tissue. The strain contrast was defined as the ratio of the average strain in the lesion to the average strain inside the background. The level of the strain contrast at the border of the lesion was found to be between -2.5 dB and -3.5 dB. The number of pixels enclosed by the corresponding isointensity contour was used to compute the total area of the thermal damage. Three sets of measurements of the area of the lesions from the elastograms were performed. The first set of measurements was obtained using a strain isointensity contour level defining the border of all lesions corresponding to -2.5 dB, the second to -3 dB and the third to -3.5 dB. Each set of measurements was separately correlated to the measured areas of gross pathology in the tissue photographs.

The extent of the lesion in the tissue photograph was also evaluated using an isointensity contour level. Because there was a sharp transition between the optical properties of the damage relative to that of the background, the determination of the level of the isointensity contour underlying the lesion was straightforward. The area of the damage was evaluated by counting the number of pixels enclosed by the isointensity contour. A pathologist reviewed the computer-generated isointensity contour levels that traced the areas of visible tissue damage in the tissue photographs. In all but 1 case of 16 evaluated, the computer-generated isointensity contour levels appeared to accurately depict the actual extent of tissue damage. In 1 case, the contour level was considered to underestimate the extent of the damage. In this case, the pathologist depicted the area of the damage manually.

Temperature and dose distribution estimations of the thermal damage

Temperature estimations were done off-line using the SPGR image data and MATLAB (Math Works, Natick, MA) data analysis software. The change in phase per unit change in temperature is approximately proportional to the product of the echo time (TE), gyromagnetic ratio (γ), field strength (B_0) and a temperature sensitivity coefficient (α_T) that represents the change in the proton resonance frequency with temperature:

$$\frac{d\phi}{dT} = TE\,\frac{d\omega}{dT} = 2\pi(\gamma B_0 TE)\alpha_T. \qquad (2)$$

Therefore, there is a linear relationship between the phase change in the MR images and the temperature change in the treatment region. The temperature sensitivity coefficient for the proton resonance frequency of

water was used ($\alpha_T = -0.01$ ppm/°C) (Hindman 1966). After the absolute tissue temperature information was obtained over time, it was used to calculate the thermal dose delivered to the tissue and to predict tissue regions of coagulative necrosis for comparison with areas of damage in tissue photographs.

A method of thermal dose estimation in cancer therapy has been developed by Sapareto and Dewey (1984) and has been suggested for use in thermal ablation therapy (Vykhodtseva et al. 1994). The effect of a variable temperature on tissue dose calculations can be expressed in terms of an equivalent time spent at 43°C using the expression:

$$t_{43} = \sum_{t=0}^{t=final} R^{(43-T_0)} \Delta t, \quad (3)$$

where t_{43} is the equivalent time at 43°C and T_0 is the average temperature during the time period Δt. The time period Δt is assumed to be small (~2% of the heating time). The quantity R equals 0.5 for temperatures greater than 43°C and 0.25 for temperatures below 43°C (Sapareto and Dewey 1984). The temporal collection of temperature maps and the Sapareto–Dewey method were used to compute the thermal dose to the tissue on a pixel-by–pixel basis under the assumption that 243 min equivalent heating at 43°C results in coagulative necrosis of the tissue.

RESULTS

Elastographic lesion visualization

Figure 2 shows matching elastograms, sonogram and tissue photograph of a cross-section from a typical HIFU-induced lesion. The cross-section is taken in a plane perpendicular to the HIFU beam. The lesion was created using an *in situ* spatially averaged focal intensity of 1565 W cm^{-2} for 20 s. The lesion area of tissue damage is depicted in the elastogram (Fig. 2a) as a very low strain region (dark) surrounded by a ring of higher strain (light gray), embedded in a soft background. Due to the large strain dynamic range between the center of the lesion and the background, the low strain contrast between the ring and the background is not clearly perceptible on a grey-scale image. The border of the lesion is better defined when the elastogram is displayed in color (Fig. 2b). As shown by Fig. 2c, the same lesion is almost imperceptible in the corresponding sonogram. At the corresponding depicted location of the lesion from the elastogram, the sonogram suggests a hypoechoic area with a poorly defined margin. The tissue photograph (Fig. 2d) shows a well-circumscribed blanched area of coagulonecrotic tissue with a centrally located darker region. The estimated areas of the lesion as measured

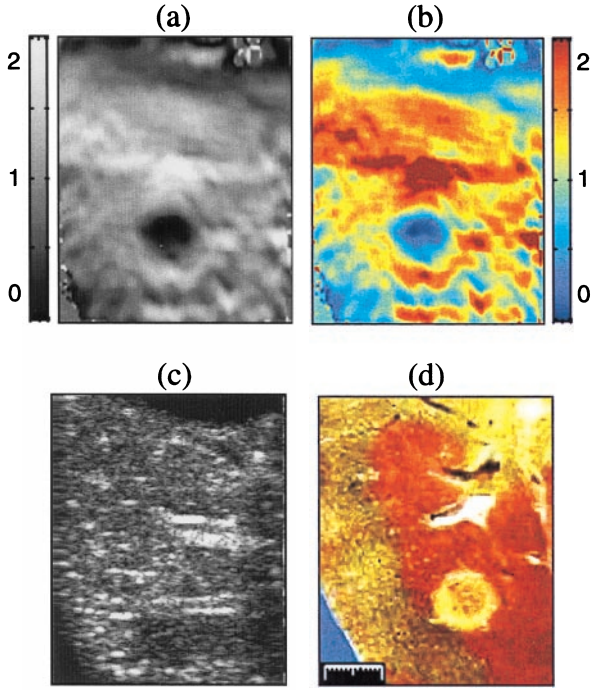

Fig. 2. Typical HIFU-induced lesion obtained at an RF power of 125 W and an exposure time of 20 s. The cross-sections are taken from a plane perpendicular to the ultrasonic treatment beam. (a) Elastogram of the lesion displayed on a grey-scale map. The lesion appears to be formed by two concentric regions: a central hard (dark) core, surrounded by a softer (lighter) ring. (b) Elastogram of (a) displayed using a color scale. The visualization in color enhances the border of the lesion. (c) Corresponding sonogram. The sonogram suggests a hypoechoic area at the corresponding location of the lesion as depicted by the elastogram. (d) Tissue photograph of the liver slice containing a well-circumscribed, tan, circular area of coagulonecrotic tissue and a darker zone of charring. The red areas in the liver specimen were a result of incomplete fixation at the time it was sliced.

from the elastogram and from the tissue photograph are 93.6 mm^2 and 100.7 mm^2, respectively, assuming a strain contrast at the border of the lesion of −2.5 dB. The slight underestimation obtained from the elastogram could be due to a possible misregistration between the planes in which the pathological measurements and elastography were performed.

Figure 3 illustrates matching elastogram, sonogram and a tissue photograph of a lesion scanned along the direction of the HIFU treatment beam. As illustrated by the elastogram and by the tissue photograph, most of the damage appears to be in regions closest to the transducer. This asymmetrical shape may be related to a variation of the attenuation coefficient and the speed of sound in the pathway of the treatment beam caused by the heat and/or the possible formation of gas bubbles (Bush et al. 1993; Chapelon et al. 1999). The estimated areas of the damage

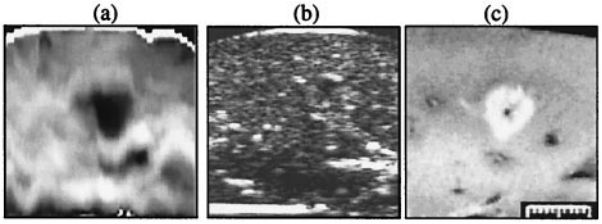

Fig. 3. Illustration of a cross-section of a HIFU-induced lesion taken from a plane parallel to the treatment beam. The lesion was induced using an RF power of 120 W for 20 s. (a) Elastogram of the lesion showing an asymmetrical shape of the damage zone along the direction of the ultrasonic beam. The treatment beam entered from the upper surface (top of the image). (b) Corresponding sonogram. (c) Tissue photograph of the same lesion.

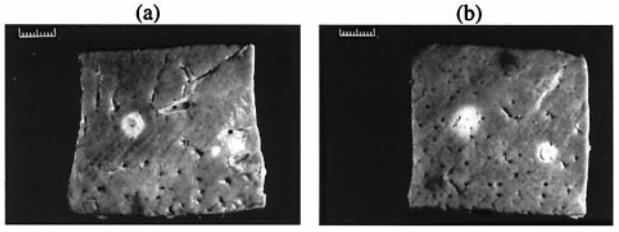

Fig. 4. Tissue photographs of the slices of liver containing the lesions that were used for mechanical testing. The two lesions were induced using RF powers of 110 W (left lesion) and 60 W (right lesion) for 20 s. The mechanical testing of the 110-W lesion was performed using the left slice and for the 60-W lesion, the measurements were taken from the right slice. The thickness of each slice was about 4 mm.

in elastography and pathology are respectively 55.2 mm^2 and 52.7 mm^2. Generally, the correlation of the elastographic and pathological measurements of the extent of the damage along the direction of the treatment beam presented larger errors when compared to the cross-sectional evaluations. Because the elastic proprieties of the tissue should not be affected by the thermal history, we attributed this discrepancy to a misregistration between the plane of the tissue photograph and the elastogram. The dimension of the lesion varies dramatically from one plane to the next, in the direction parallel to the HIFU beam. In contrast, the lesion is generally longer across the treatment beam and, therefore, may maintain a constant shape and size for a relatively large depth. This will result in less errors associated with any misregistration between the transverse planes across the ultrasound beam axis in the elastogram and the corresponding tissue photograph. This hypothesis is confirmed from observations that larger lesions are typically visible in several contiguous transverse slices across the ultrasound beam axis, and they appear in fewer slices if scanned and cut longitudinally along the beam axis.

Lesion contrast evaluation

Figure 4 shows photographs of two slices where two lesions are visible. The mechanical testing of each lesion was performed using the slice where the lesion appeared to have its biggest dimension. The results of the mechanical testing are illustrated in Fig. 5. This figure shows the stress-strain curves obtained in the surrounding healthy tissue and in each lesion. The first curve (C1) corresponds to the healthy tissue; the second one (C2) to the 60-W lesion and the third one (C3) to the 110-W lesion. In all cases over a small strain range (less than 3%), the measured strain changes almost linearly with the applied stress. This suggests that, within this small strain range where elastograms were acquired, the stress/strain relationship is approximately linear. Consequently, the elastic modulus (slope of the stress/strain curve) is constant over this strain range. As expected, the elastic modulus decreases from the high power lesion to the second lesion and, finally, to the healthy tissue. The 110-W lesion is about 3.6 times stiffer, and the 60-W lesion is approximately 1.4 times stiffer than the healthy tissue.

Figure 6 shows the elastograms of the 110-W lesion and the 60-W lesion, respectively. For a better appreciation of the strain contrast between the lesions and the background, the strain profiles taken from the elastograms of Fig. 6a and b at a depth crossing the center of

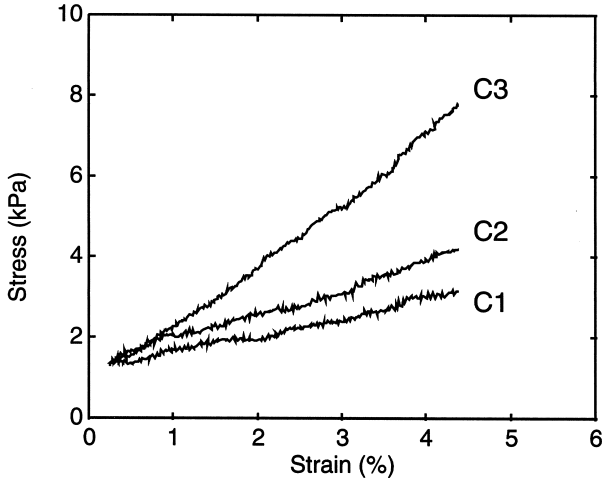

Fig. 5. Stress/strain curves of the healthy tissue (C1), of the 60-W lesion (C2) and of the 110-W lesion (C3). The three curves suggest a linear stress-strain relationship within a small range of applied strain. The elastic modulus (slope of the stress/strain curve) decreases from the high power lesion, which is 3.6 times stiffer than the healthy tissue, to the second lesion, approximately 1.4 times stiffer than the healthy tissue, to the healthy tissue.

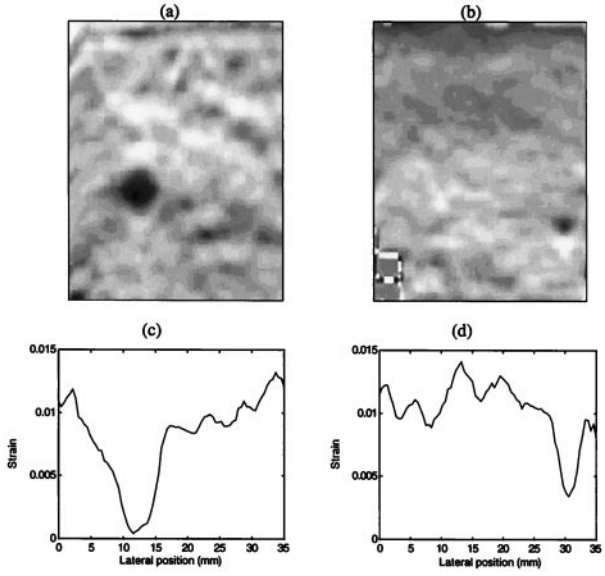

Fig. 6. Elastograms of the lesions shown in Fig. 4. (a) Elastogram of the 110-W lesion. The average strain in the dark area inside the lesion is 5 times smaller than the average strain in the background. On the average the entire lesion is about 2 times harder than the background. (b) Elastogram of the 60-W lesion. The average strain inside the entire lesion is approximately 1.6 times smaller than the average strain in the healthy tissue. (c) Strain profile from the elastogram of the 110-W lesion taken laterally across the center of the lesion. (d) Strain profile from the elastogram of the 60-W lesion taken laterally across the center of the lesion.

the lesions are shown in Fig. 6c and d. The average strain inside the dark area of the 110-W lesion is 5 times smaller than the average strain in the background. The entire lesion is approximately 2 times stiffer than the background. The average strain inside the entire 60-W lesion is approximately 1.6 times smaller then the average strain in the background. Due to the contrast-transfer–efficiency (CTE) limitation (Ponnekanti et al. 1995; Kallel et al. 1996), for the 110-W and the 60-W lesions, the average elastic modulus of the entire damage areas would respectively be about 3 and 2.2 times larger compared to the healthy tissue. This is assuming a plane strain state of a cylindrical inclusion bounded by an infinite background. The elastic modulus contrast predicted from the elastograms did not correlate precisely with the contrast measured using the Instron testing machine. This is due to two considerations. First, the variation of the modulus inside the lesion relative to the size of the indentor used to make the measurements relative to the dimension of the lesion. And second, the composite nature of the modulus that was calculated from the Instron data compared to the finer resolution possible with the elastogram. In other words, the stiffness computed from the Instron data represents the elastic modulus of the entire thickness of the sample—a composite value that includes the modulus of the lesion and the modulus of the surrounding tissue. The composite stiffness represents the proportionate contribution of the lesion and the surrounding tissue to the thickness of the test sample.

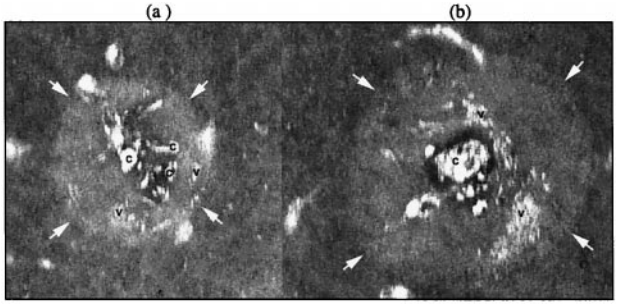

Fig. 7. Photomicrographs of two lesions induced at an RF power of (a) 80 W and (b) 120 W for 15 s. Circular areas of coagulative necrosis (arrows) with centrally located regions containing (c) irregular cavities and (v) vacuolization. Hematoxylin and eosin stain, magnification ×25.

Histological characterization of the tissue damage

Two typical lesions (Fig. 7) that were created using an *in situ* spatially averaged focal intensity of 1503 W cm^{-2} for 15 s and 1002 W cm^{-2} for 10 s, were evaluated histopathologically. Both lesions consisted of well-circumscribed areas of coagulative necrosis with centrally located regions containing large irregular cavities, surrounded by midcentral zones containing smaller vacuoles. The dimensions of the central region in the high-power lesion were larger than in the low-power lesion.

Temperature profile and strain contrast

Figure 8 shows the elastograms and corresponding thermal dose distributions of a typical lesion in two parallel planes, spaced by 1 mm. Observe that the shape and size of the lesion, as depicted from the elastograms, are consistent with the corresponding shape and size as represented by the thermal dose distributions. The temperature and the strain profiles in the center of the same lesion are plotted in Fig. 9. All the curves were obtained by averaging four profiles taken at the center of the lesion. The error bars represent the SD of the average of the four strain and temperature profiles. As it can be noticed, the estimated temperature in the first plane (Fig. 9b, upper curve) exceeded 100°C, resulting in tissue vaporization, and in the second plane (Fig. 9b, lower curve), the maximum estimated temperature reached was 80°C. As expected, the strain contrast inside the first plane (Fig. 9a, lower curve) is considerably larger than that of the second plane (Fig. 9a, upper curve). This

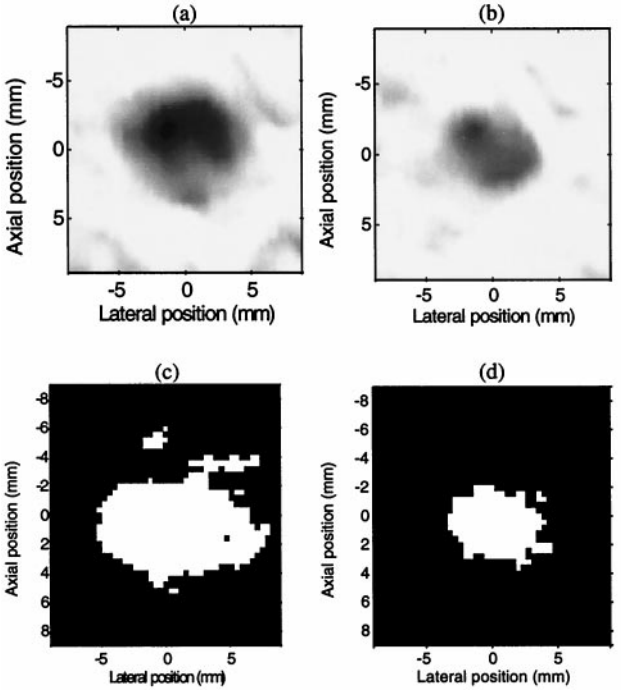

Fig. 8. Elastograms and corresponding thermal dose distributions of the lesion shown in Fig. 2, taken in two different planes perpendicular to the HIFU beam. (a) Elastogram of the lesion, taken in the plane of its biggest dimension. (b) Elastogram of the lesion, taken in a plane 1 mm distal from the plane imaged in (a). (c) Thermal dose distribution of the lesion in the plane shown in (a). (d) Thermal dose distribution of the lesion in the plane shown in (b). The estimated areas of the damages from the elastograms and the corresponding thermal dose distributions are, respectively, 93.64 mm^2 and 86.65 mm^2 for the first plane, 41.3 mm^2 and 38 mm^2 for the second plane.

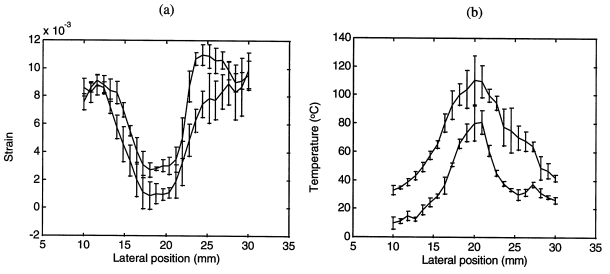

Fig. 9. Horizontal strain and estimated temperature profiles from the lesion shown in Fig. 8. (a) Strain profiles taken at the center of the lesion from the two elastograms. The two profiles represent an average over 4 adjacent strain profiles taken around the center of the lesion. (b) Estimated temperature profiles taken in the center of the lesion in the two planes in which the dose distributions of Fig. 8b and d were evaluated. The two profiles were obtained by averaging 4 temperature profiles around the center of the lesion. The error bars show the standard deviation around the average of the 4 profiles. For the strain profiles, the lower curve is referred to the plane of the biggest dimension of the lesion; for the temperature profiles, the upper curve is referred to the plane of the biggest dimension of the lesion.

suggests that elastography may ultimately be useful in distinguishing between the different degrees of tissue damage as depicted histologically (Fig. 7).

Three-dimensional extent of the lesion

Figure 10 shows a series of elastograms and matching sonograms from a typical lesion obtained from parallel 1-mm equally spaced cross-sections. The cross-sections were taken in planes perpendicular to the HIFU beam. The lesion is clearly visible in all the elastograms, with different dimensions depending on the position of the plane relative to the depth of the focal spot. In contrast, the lesion is not clearly depicted by the corresponding sonograms. Figure 11 shows the strain profiles, plotted on a logarithmic scale, taken laterally from the four elastograms (Fig. 10) at the center of the lesion. As it can be noticed from Fig. 11, the strain contrast inside the lesion compared to the background changes slowly in the first two planes and in the last one. However, the strain contrast abruptly increases in the third plane, the change being more than 1 order of magnitude. This might suggest that, at this depth, the biggest deposition of acoustic energy occurred and, consequently, the temperature reached its highest values.

Figure 12 shows a series of elastograms and corresponding sonograms from the same lesion shown in Fig. 10, but which were obtained from cross-sections taken from planes parallel to the HIFU beam. The cross-sections are equally spaced by 1 mm. The lesion is clearly depicted in every elastogram, with different dimensions

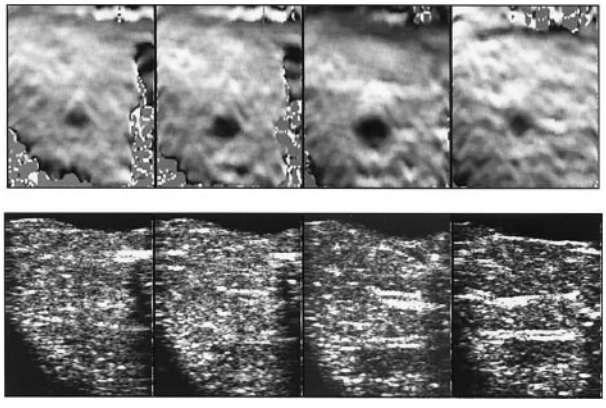

Fig. 10. Elastograms and corresponding sonograms of the lesion shown in Fig. 1. The cross-sections are obtained from 1-mm, equally spaced parallel planes, perpendicular to the HIFU beam. The size of the lesion changes from one plane to another, being maximum in the third plane. The lesion is not clearly depicted in the corresponding sonograms.

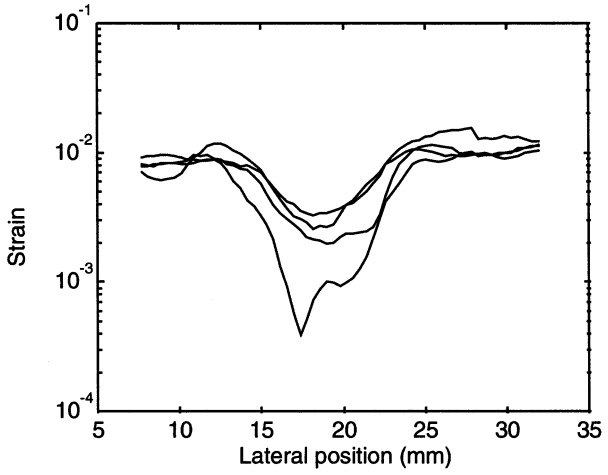

Fig. 11. Strain profiles plotted on a semilogarithmic scale and taken from the 4 elastograms illustrated in Fig. 10 at the center of the lesion. The lesion/background strain contrast increases abruptly in the plane where the lesion appears with its biggest dimension.

depending on the position of the plane relative to the axis of the HIFU beam. The lesion appears to be depicted by the corresponding sonograms as a slightly hyperechoic area. It is interesting to notice that in this case, as shown by Figs. 10 and 12, the ultrasonic depiction of the same lesion depends on the orientation of the imaging ultrasonic beam relative to the HIFU beam. Figure 13 shows the strain profiles, plotted on a semilogarithmic scale, taken laterally from the four elastograms at the center of the lesion. As in Fig. 11, observe that, in one plane, the strain contrast increases abruptly, suggesting the biggest acoustic energy deposition. From Figs. 11 and 13, we notice that, on the average, the lesion is depicted with similar strain contrast, suggesting that the lesion/background strain contrast tends to be isotropic.

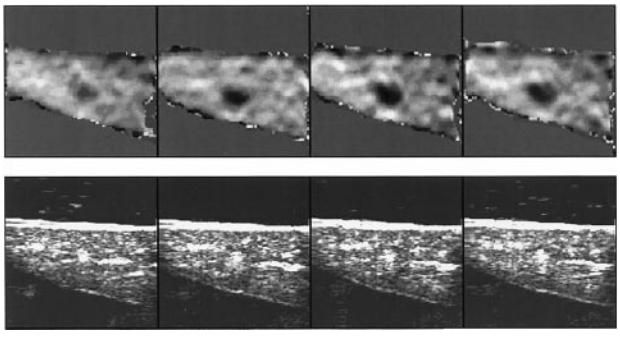

Fig. 12. Elastograms and corresponding sonograms of the lesion shown in Fig. 1. The cross-sections are obtained from 1-mm equally spaced parallel planes, parallel to the axis of the HIFU beam.

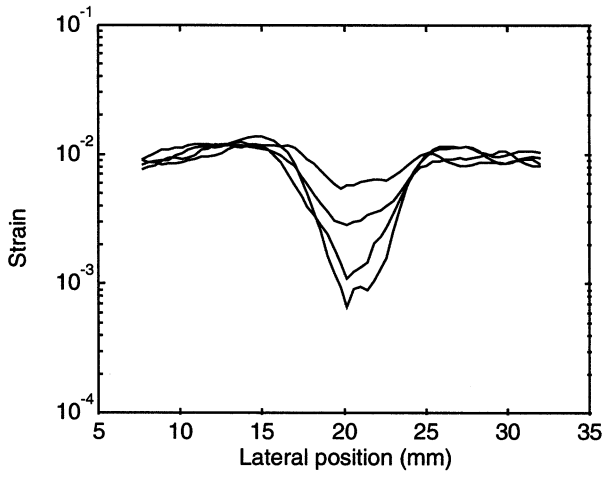

Fig. 13. Horizontal strain profiles, plotted on a semilogarithmic scale, taken at the center of the lesion from the four elastograms illustrated in Fig. 12.

Elastographic visualization of multiple lesions

Figures 14 and 15 show elastograms, sonograms and tissue photographs of an array of two and three lesions, respectively. From Fig. 14, it is interesting to notice that the sonogram clearly depicts the right lesion as a hyperechoic area. The high echogenicity of this lesion could be related to the formation of gas bubbles due to vaporization and/or cavitation. However, the extent of the lesion is seriously underestimated by the sonogram, but elastographic and pathological measurements are in good agreement for both lesions. The elastogram of Fig. 15a clearly shows the three small lesions as they appear in the corresponding tissue photograph. This demonstrates good agreement between elastography

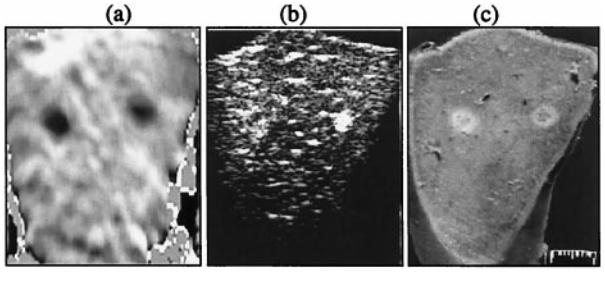

Fig. 14. Matching (a) elastogram, (b) sonogram, and (c) tissue photograph of a pair of two lesions created using RF power of 110 W for 15 s. The estimated areas of the lesions from the elastogram and the tissue photograph are 33.84 mm^2 and 31.6 mm^2 for the left lesion, 29.03 mm^2 and 33.86 mm^2 for the right lesion, respectively. The corresponding sonogram clearly depicts the right lesion as a small hyperechoic zone. The evaluation of the hyperechoic area visible in the sonogram corresponds to 12.5 mm^2.

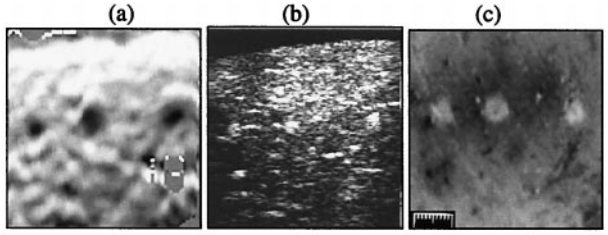

Fig. 15. Matching (a) elastogram, (b) sonogram and (c) tissue photograph of an array of three lesions, all of them induced using RF power of 90 W for 12 s. The elastogram and tissue photograph depict the three small lesions with approximately the same size and relative location.

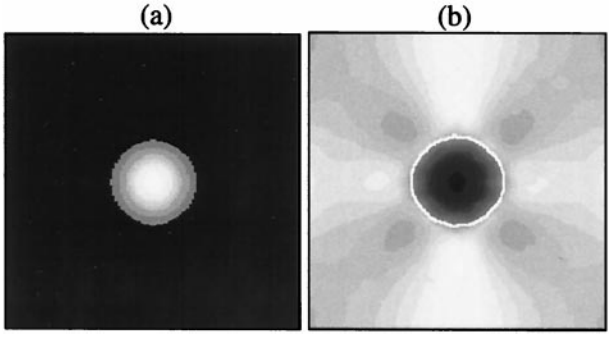

Fig. 16. (a) Modulus distribution and (b) corresponding strain image used to define the level of strain contrast at the border of the lesion. The modulus of the inclusion follows a Gaussian distribution. The ROI is 40×40 mm^2. The maximum diameter is 12.5 mm. The contour line superimposed on the strain image corresponds to strain-contrast level of -2.5 dB with respect to the background.

and gross tissue pathology, not only in the evaluation, but also in the localization of the damage inside the tissue. These three lesions are not clearly visible in the sonogram (Fig. 15b).

Lesion evaluation

The automatic evaluation of the area of the lesion depends on the accuracy of the selection of the isointensity contour strain level. In the following section, finite element (FE) simulation results supporting our choice of this isointensity contour level are presented. The FE analysis was performed using a commercial software package (ALGOR, Inc., Pittsburgh, PA).

The simulation consisted of using three different finite element models (FEM). The first model consisted of an 8-mm diameter inclusion, 1.8 times stiffer than the background. The second model consisted of a 6-mm diameter inclusion surrounded by an 8 mm diameter ring. The inclusion was 6 times stiffer than the background and the ring was 1.8 times stiffer than the background. The third model consisted of an inclusion with a modulus distribution following a Gaussian distribution with a 3.5-mm spatial SD and a maximum modulus contrast reached in the center of the lesion of 30. This permitted us to evaluate the strain contrast at the border of the inclusion in three typical situations: a lesion formed by a single region, a lesion formed by a solid core surrounded by a softer ring, and a lesion in which the modulus distribution follows a Gaussian distribution. Figure 16a shows the modulus distribution of the third model in an ROI of 40×40 mm^2. Figure 16b shows the corresponding strain image resulting from a uniform uniaxial compression of 1%. The isointensity contour level underlying the extent of the entire lesion is superimposed on the strain image. This level corresponds to a strain contrast of -2.5 dB.

To define the strain contrast level at the border of the lesion, we estimated, from the simulated strain image, the area enclosed inside the strain isointensity contour levels corresponding to a strain lesion/background contrast ranging from -1.5 dB to -5 dB by steps of 0.5 dB between two consecutive levels. These measurements were compared to the area as depicted from the corresponding modulus distributions. This procedure was performed for all three simulation studies. The results demonstrated that, to maintain a measurement error of less than 5%, the level of strain-contrast defining the border of the lesion had to be chosen between -2.5 dB and -3.5 dB. Outside this range, the area was over- or underestimated with an error of more than 5%.

Figure 17 shows an elastogram and the corresponding gross pathology photograph of a typical lesion. The isointensity contour level underlying the extent of the thermal damage is superimposed on the elastogram. This level corresponds to a strain contrast of -2.5 dB. For the lesion shown in Fig. 8 (in both planes), we found that the area enclosed by this selected isointensity contour level in the elastogram matched the extent of the lesion as depicted from the thermal dose distribution, with an error within 5%. As shown by Fig. 2a, when the elastogram is displayed using a gray-scale map, to a human observer the boundaries of the damage are not clearly distinguishable from the background. When the elastogram is displayed in color, the lesion margins are better depictable from the background (Fig. 2b). As shown in Fig. 17a, the isointensity contour level clearly depicts the lesion, resulting in good correlation in size and shape with the lesion as it appears in the photograph of the tissue slice (Fig. 17b).

The automatic evaluation of the damaged area was applied to a total of 16 lesions. Figure 18 shows a scatter diagram of the areas of tissue damage as determined from photographs of the tissue slices vs. the areas as depicted from the corresponding elastograms in the case

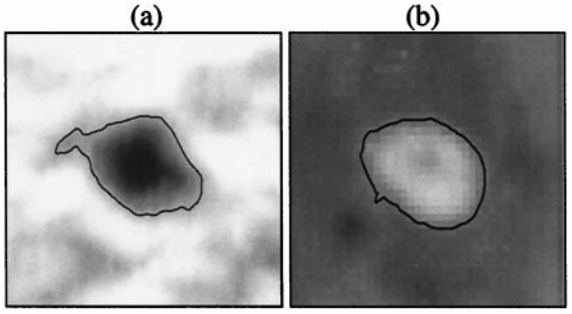

Fig. 17. Illustration of the computer-generated evaluation of the damaged area using the elastogram and the tissue photograph. The lesion was created using an RF power of 80 W for 15 s. (a) Grey-scale elastogram of the lesion. The isointensity contour level corresponding to a strain contrast level of −2.5 dB and defining the border of the lesion is superimposed on the elastogram. (b) Tissue photograph of the corresponding liver slice. The computer-generated boundary of the area of tissue damage is depicted. The pathology photograph is cropped around the lesion, to be in good registration with the elastogram of Fig. 16a. The estimated areas delimited by the two contours are approximately 39 mm^2 from the elastogram and 38 mm^2 from the pathology photograph.

of −2.5 dB strain contrast at the border of the lesion. The same measurements were repeated also in the case of strain levels defining the lesions of −3 dB and −3.5 dB. The coefficient of determination r^2 of the linear regression fit to the data is dependent on the level of strain

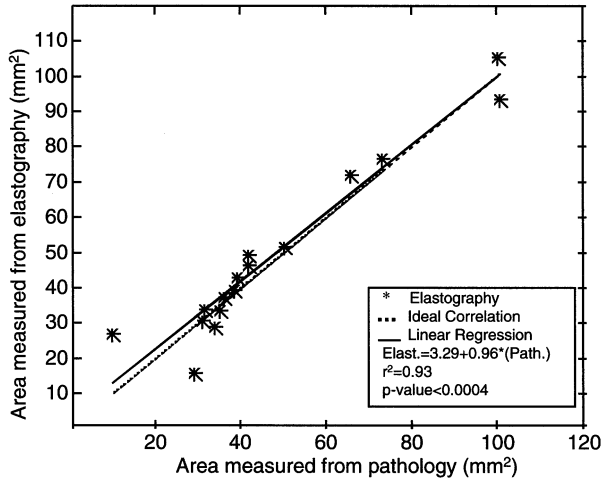

Fig. 18. Scatter plot of the area of the HIFU-induced lesions as evaluated using elastography vs. the area of tissue damage as measured from the photographs of the corresponding liver slices. The automatic evaluation of the damage zone was applied to a total of 16 lesions; the r^2 value from the statistical regression analysis is 0.93 for the 16 data points used in this study. The corresponding p value is <0.0004. Both ideal and fitted regression lines are shown.

contrast used to define the lesion automatically. For the three values considered, the r^2 values were 0.93 for the measurements obtained with −2.5 dB and 0.91 for the other two cases. The corresponding p values were <0.0004 for all three measurements. It is noteworthy that, if we neglect the less reliable contribution of the smallest lesion, that is about 10 mm^2 and, hence, close to the resolution limit of elastography, we obtain an r^2 value of 0.95, p value < 0.0004 and a regression equation of ($n = 15$):

$$(\text{Elast.}) = -1.05 + 1.03*(\text{Path.}). \quad (4)$$

This equation demonstrates an intercept close to zero and a slope that is very close to one.

DISCUSSION

Statistical analysis of the estimation of the area of tissue damage induced by high-intensity focused ultrasound in excised canine liver specimens reveals high correlation between elastographic and gross pathological measurements. The results of our experiments were obtained considering the hypothetical existence of a strain contrast threshold, empirically found to be between −2.5 dB and −3.5 dB, defining the border of a HIFU-induced lesion. To validate this threshold, mechanical testing measurements were performed and compared to the elastographic measurements. In addition, temperature mapping and thermal dose distributions were used to confirm the validity of this threshold. The ability of elastography to image low modulus contrast was previously demonstrated (Kallel et al. 1998), as well as the possibility of detecting thermal damage induced in soft tissue (Stafford et al. 1998). Therefore it is not surprising that it is possible to accurately detect the low hypothetical strain contrast threshold defining the border of the lesions in the current study. We believe that the high correlation obtained in this study was achieved due to the objectivity of the automatic computer-generated isointensity contours for the evaluation of the extent of the damaged tissue. The lesion extent evaluation by a human observer is subjective and may be affected by many factors, such as the monitor type and its setting. In contrast, the automatic evaluation is objective and does not depend on the display parameters. Moreover, the choice of the area instead of the diameter (Stafford et al. 1998) as the parameter to correlate permitted a significant reduction of the measurement errors.

The plot of Fig. 18 shows a significant discrepancy between elastography and pathology in the evaluation of the area of the smallest lesion considered in this study. In the tissue photograph, the diameter of the smallest lesion was approximately 3.4 mm. The limited elastographic

and ultrasonic spatial resolutions could explain the discrepancy between elastography and pathology for such a small lesion. The use of a higher imaging transducer center frequency may result in an improvement of the precision of the elastographic detection and evaluation of smaller lesions.

Several authors reported on HIFU experiments conducted on liver tissue, especially because of the widespread worldwide incidence of liver cancer and death from liver metastases (Malcolm and ter Haar 1997; Tavakkoli et al. 1997; Clarke and ter Haar 1997; Chen et al. 1997). Because elastography in its current developmental stage is not used for *in vivo* imaging of the liver, for the purpose of this study, the liver was selected as a model mostly because of its good optical properties. Moreover, the liver is assumed to be an elastically homogeneous tissue. The current primary diagnostic imaging applications of elastography are breast and prostate cancer. Therefore, this study has to be considered as preliminary and future experiments are required to investigate the performance of elastography for evaluating HIFU-induced lesions in these more heterogeneous tissue types.

The possibility of detecting small changes in the tissue elastic properties is mostly due to the high CNR provided by elastography (Varghese and Ophir 1998). This may also explain one of the advantages of elastography over standard sonography in evaluating thermal lesions. It has been shown that, for identical object contrasts, elastography has a significantly higher detectability when compared to sonography (Belaid et al. 1994). From this point of view, elastography overcomes the limitations of standard sonography in the evaluation of the boundary of necrotic tissue volumes. The elastographic CNR of HIFU lesions may also be significantly improved by using subtraction techniques.

We have shown that the geometrical extent of a typical lesion, as depicted by the elastograms in two planes, is in good agreement with its geometrical extent as depicted from the corresponding thermal dose distributions obtained by MRI (Figs. 8 and 9). The elastographic appearance of the lesion in the first plane suggests the presence of a stiff core (dark gray) at the center of the lesion. In the second plane, the lesion appears in the elastogram as a uniform light gray region. The strain contrast in the center of the lesion in the first plane is significantly higher compared to the same lesion in the second plane (Fig. 9). Because the temperature in the lesion in the first plane exceeded 100°C, different mechanisms of damage may have been involved in the formation of this lesion. It is known that the mechanical mechanism of damage is more violent than the thermal one, inducing much more dramatic changes in the mechanical properties of the tissue. Consequently, the formation of the core inside the first lesion might be related to the occurrence of vaporization and/or cavitation effects. Histopathological evaluation of the specimens revealed central formation of irregular cavities and surrounding midzonal formation of vacuoles (vaporization). The finite resolution of the elastographic system may also have an affect on the dimensions and appearance of this central area.

Because changes in the strain contrast follows temperature variations (Fig. 9), it will be of interest to investigate the relationship that may exist between strain contrast and temperature elevation during the formation of a HIFU-induced lesion. From the previous discussion, this hypothetical relationship should, in principle, vary by changing from the case of purely thermal lesions to the case of lesions generated by a combination of mechanical and thermal mechanisms of damage.

CONCLUSION

We have shown that elastography is able to accurately depict the size and position of lesions induced by high-intensity focused ultrasound in soft tissues. The statistically significant high correlation between elastographic and actual measurements of the tissue lesion suggests that elastography may be a very reliable method for the estimation and characterization of HIFU-induced lesions and, therefore, may overcome the known limitations of standard ultrasonic techniques for monitoring focused ultrasound-based surgery procedures.

Acknowledgements—Supported by National Institutes of Health (USA) Program Project grant P01-CA64597 to the University of Texas Medical School. The authors acknowledge Michael Brennan and John Frederick from the department of anesthesiology of The University of Texas Houston for harvesting the tissue samples. We thank Prof. Tortoli for his helpful comments, Elisa Konofagou for discussions and contribution to the measurements and Alex Alaniz for discussions on properties of proteins.

REFERENCES

Belaid N, Céspedes EI, Thijssen JM, Ophir J. Lesion detection in simulated elastographic and elastographic images: a psychophysical study. Ultrasound Med Biol 1994;20:877–891.

Bilgen M, Insana MF. Predicting target delectability in acoustic elastography. IEEE Ultrason Sympos 1997;2:1427–1430.

Bush NL, Rivens I, ter Haar GR, Bamber JC. Acoustic properties of lesions generated with an ultrasound therapy system. Ultrasound Med Biol 1993;19:789–801.

Cathignol D, Birer A, Nachef S, Chapelon JY. Electronic beam steering of shock waves. Ultrasound Med Biol 1995;21:365–377.

Chapelon JY, Ribault M, Vernier F, Souchon R, Gelet A. Treatment of localised prostate cancer with transrectal high intensity focused ultrasound. Eur J Ultrasound 1999;9:31–38.

Chen L, ter Haar GR, Hill CR. Influence of ablated tissue on the formation of high-intensity focused ultrasound lesions. Ultrasound Med Biol 1997;23:921–931.

Chen SS, Humphrey JD. Heat-induced changes in the mechanics of a collagenous tissue: pseudoelastic behavior at 37°C. J Biomech 1998;31:211–216.

Chung AH, Hynynen K, et al. Optimization of spoiled gradient-echo phase imaging for in vivo localization of a focused ultrasound beam. Magn Reson Med 1996;36:745–752.

Clarke RL, ter Haar GR. Temperature rise recorded during lesion formation by high-intensity focused ultrasound. Ultrasound Med Biol 1997;23:299–306.

Cline HE, Hynynen K, Hardy CJ, Watkins RD, Schenck JF, Jolesz FA. MR temperature mapping of focused ultrasound surgery. Magn Reson Med 1994;31:628–636.

Cline HE, Hynynen K, Watkins RD, Adams WJ, Schenck JF, Ettinger RH, Freund WR, Vetro JP, Jolesz FA. Focused US system for MR imaging-guided tumor ablation. Radiology 1995;194:731–737.

Cline HE, Schenck JF, Hynynen K, Watkins RD, Souza SP, Jolesz FA. MR-guided focused ultrasound surgery. J Comput Assist Tomogr 1992;16:956–965.

Cline HE, Schenck JF, et al. Magnetic resonance-guided thermal surgery. Magn Reson Med 1993;35:62–71.

Consigny PM, Teitelbaum GP, Gardiner GG, Kerns WD. Effects of laser thermal angioplasty on arterial contractions and mechanics. Cardiov Interven Radiol 1989;12:83–87.

Corry PM, Jabboury K, Armour EP, Kong JS. Human cancer treatment with ultrasound. IEEE Trans Sonics Ultras 1984;31:444–456.

Fasano VA, Ponzio RM, Benech F, Sicuro M. Effects of laser sources (Argon, Nd: YAG, CO_2) on the elastic resistance of the vessel wall. Lasers Surg Med 1983;2:45–54.

Fry WJ, Fry FJ. Fundamental neurological research and human neurosurgery using intense ultrasound. IRE Trans Med Electron 1960; ME-7:166–181.

Fry FJ, Johnson LK. Tumor irradiation with intense ultrasound. Ultrasound Med Biol 1978;4:337–341.

Fry WJ, Mosberg WH, Barnard JW, Fry FJ. Production of focal destructive lesions in the central nervous system with ultrasound. J Neurosurg 1954;11:471–478.

Fry WJ, Wulff VJ, Tucker D, Fry FJ. Physical factors involved in ultrasonically induced changes in living system. J Acoust Soc Am 1950;22:867–876.

Gao L, Parker KJ, Lerner RM, Levinson SF. Imaging of the elastic properties of tissue—A review. Ultrasound Med Biol 1996;22: 959–977.

Garra BS, Céspedes I, Ophir J, Spratt S, Zurbier RA, Magnant CM, Pennanen MF. Elastography of breast lesions: initial clinical results. Radiology 1997;202:79–86.

Gertner MR, Wilson BC, Sherar MD. High-frequency ultrasound properties of multicellular spheroids during heating. Ultrasound Med Biol 1998;24:461–468.

Gertner MR, Wilson BC, Sherar MD. Ultrasound properties of liver tissue during heating. Ultrasound Med Biol 1997;23:1395–1403.

Hill CR, ter Haar GR. High intensity focused ultrasound—potential for cancer treatment. Br J Radiol 1995;68:1296–1303.

Hill CR, Rivens I, Vaughan MG, ter Haar GR. Lesion development in focused ultrasound—potential for cancer treatment. Br J Radiol 1995;68:1296–1303.

Hill CR, Rivens I, Vaughan MG, ter Haar GR. Lesion development in focused ultrasound surgery: a general model. Ultrasound Med Biol 1994;20:259–269.

Hindman JC. Proton resonance shift of water in the gas and liquid states. J Chem Phys 1966;44:4582–4592.

Hynynen K. Focused ultrasound surgery guided by MRI. Sci Med 1996;3:62–71.

Hynynen K. Review of ultrasound therapy. IEEE Ultrasonics Symp 1997;2:1305–1313.

Hynynen K. The threshold for thermally significant cavitation in dog's thigh muscle *in vivo*. Ultrasound Med Biol 1991;17:157–169.

Hynynen K, Freund WR, Cline HE, Chung AH, Watkins RD, Vetro JP, Jolesz FA. A clinical, noninvasive, MR imaging-monitored ultrasound surgery method. Radiographics 1996;16:185–195.

Kallel F, Bertrand M, Ophir J. Fundamental limitations on the contrast-transfer efficiency in elastography: An analytical study. Ultrasound Med Biol 1996;22:463–470.

Kallel F, Ophir J, A least-squares strain estimator for elastography. Ultrason Imaging 1997;19:195–208.

Kallel F, Ophir J, Magee K, Krouskop T. Elastographic imaging of low-contrast elastic modulus distributions in tissue. Ultrasound Med Biol 1998;24:409–425.

Kallel F, Stafford RJ, Price RE, Righetti R, Ophir J, Hazle JD. The feasibility of elastographic visualization of HIFU-induced thermal lesions in soft-tissues. Ultrasound Med Biol 1999;25:641–647.

Kang T, Resar J, Humphrey JD. Heat-induced changes in the mechanical properties of passive coronary arteries. ASME J Biomech Eng 1995;117:86–93.

Krouskop TA, Wheeler TM, Kallel F, Garra BS, Hall T. The elastic moduli of breast and prostate tissues under compression. Ultras Imag 1998;20:260–274.

Lele PP. Concurrent detection of the production of ultrasonic lesions. Med Biol Eng 1966;4:451–456.

Lele PP. Advanced ultrasonic techniques for local tumor hyperthermia. Radiol Clin North Am 1989;27:559–575.

Lele PP. Production of deep focal lesions by focused ultrasound-current status. Ultrasonics 1967;5:105–122.

Lynn JG, Putnam TJ. Histological and cerebral lesions produced by focused ultrasound. Am J Pathol 1944;20:637–649.

Malcolm AL, ter Haar GR. Ablation of tissue volumes using high intensity focused ultrasound. Ultrasound Med Biol 1996;22:659–669.

McKenzie AL. Physics of thermal processes in laser-tissue interaction. Phys Med Biol 1990;35:1175–1209.

Moreno R, Damianou C, Sanghvi N. Tissue temperature estimation in-vivo with pulse-echo. IEEE Ultras Symp 1995;2:1225–1229.

Norberg M, Haggman M, Anderson T, Bush C, Magnusson A. Evaluation of localised prostate cancer: a comparative study of transrectal ultrasonography versus histopathology. Eur Radiol 1993;3: 166–173.

Ophir J, Céspedes EI, Ponnekanti H, Yazdi Y, Li X. Elastography: a quantitative method for imaging the elasticity of biological tissues. Ultrasonics Imaging 1991;13:111–134.

Ponnekanti H, Ophir J, Huang Y, Céspedes I. Fundamental mechanical limitations on the visualization of elasticity contrast in elastography. Ultrasound Med Biol 1995;21:533–543.

Prat F, Chapelon JY, Abou El Fadil F, et al. Focused liver ablation by cavitation in the rabbit: a potential new method of extracorporeal treatment. Gut 1994;35:395–400.

Prat F, Ponchon T, Berger F, et al. Hepatic lesions in the rabbit induced by acoustic cavitation. Gastroenterology 1991;100:1345–1350.

Ribault M, Chapelon JY, Cathignol D, Gelet A. Differential attenuation imaging for the characterization of high intensity focused ultrasound lesions. Ultrasonic Imaging 1998;20:160–177.

Sanghvi NT, Fry FJ, Bihhrle R, Foster RS, Phillips MH, et al. Non invasive surgery of prostate tissue by high-intensity ultrasound. IEEE Trans Ultras Ferroelec Freq Contr 1996;43:1099–1110.

Sapareto SA, Dewey WC. Thermal dose determination in cancer therapy. Int J Radiat Oncol Biol Phys 1984;10:787–800.

Sarvazyan AP. Shear acoustic properties of soft biological tissues in medical diagnostics. (Abstr.) J Acoust Soc Am Proc 1993;93:23–29.

Seip R, Ebbini E. Non-invasive estimation of tissue temperature response to heating fields using diagnostic ultrasound. IEEE Trans Biomed Eng 1995;42:829–839.

Simon C, Van Baren P, Ebbini E. Two-dimensional temperature estimation for ultrasound thermotherapy using diagnostic ultrasound. IEEE Trans UFFC 1998;45:1088–1099.

Stafford RJ, Kallel F, Price RE, Cromeens DM, Krouskop TA, Hazle JD, Ophir J. Elastographic imaging of thermal lesions in soft tissue: a preliminary study *in vitro*. Ultrasound Med Biol 1998;24:1149–1458.

Straube W, Arthur R. Theoretical estimation of the temperature dependence of backscattered ultrasonic power for non-invasive thermometry. Ultrasound Med Biol 1994;20:915–922.

Tavakkoli J, Birer A, Arefiev A, Prat F, Chapelon JY, Cathignol D. A piezocomposite shock wave generator with electronic focusing capability: application for producing cavitation-induces lesions in rabbit liver. Ultrasound Med Biol 1997;23:107–115.

ter Haar GR. Ultrasound focal beam surgery. Ultrasound Med Biol 1995;21:1089–1100.

ter Haar GR, Sinnett D, Rivens I. High intensity ultrasound-A surgical technique for the treatment of discrete liver tumors. Phys Med Biol 1989;34:1743–1750.

Ueno S, Hashimoto M, Fukukita H, Yano T. Ultrasound thermotherapy in hyperthermia. IEEE Ultras Symp 1990;2:1645–1652.

Varghese T, Ophir J. An analysis of elastographic contrast-to-noise ratio. Ultrasound Med Biol 1998;24:915–924.

Vykhodtseva NI, Hynynen K, Damianou C. Pulse duration and peak intensity during focused ultrasound surgery: theoretical and experimental effect in rabbit brain *in vivo*. Ultrasound Med Biol 1994; 20:987–1000.

Watkin NA, ter Haar GR, Morris SB, Woodhouse CRJ. The urological applications of focused ultrasound surgery. Br J Urol 1995; 75(Suppl.1):1–8.

Wells PNT. Biomedical ultrasonics. London, New York: Academic Press, 1977.

Yang R, Kopecky KK, Rescorla FJ, Galliani CA, Wu EX, Grosfeld J. Sonographic and computed tomography characteristics of liver ablation lesions induced by high intensity focused ultrasound. Invest Radiol 1993;28:796–801.